

# Remote Sensing of Sea Surface Temperature Using AMSR-2 Measurements

Suleiman Odeh Alswiss, *Member, IEEE*, Zorana Jelenak, *Member, IEEE*, and Paul S. Chang, *Member, IEEE*

**Abstract**—In this paper, an operational retrieval algorithm is described to infer sea surface temperature (SST) using measurements from the Advanced Microwave Scanning Radiometer-2 (AMSR-2) aboard the Global Change Observation Mission-Water. The algorithm exploits AMSR-2 observations from 12 channels (6–36 GHz, horizontally and vertically polarized), after being corrected for residual calibration biases, to retrieve SST using a statistical based scheme. The Algorithm performance is assessed and results are compared to models and other independent data products.

**Index Terms**—Advanced microwave scanning radiometer-2 (AMSR-2), brightness temperature, global change observation mission-water (GCOM-W1), microwave, radiometer, sea surface temperature (SST).

## I. INTRODUCTION

SEA SURFACE TEMPERATURE (SST) is an essential component to understand air-sea interaction and climate variability. It plays a fundamental role in the energy and moisture exchange between oceans and the atmosphere. A clear demonstration of the coupling between ocean surface geophysical parameters and the atmosphere is the recurring El Niño and La Niña cycles [1], [2]. Moreover, SST influences the development of extreme wind events such as hurricanes and tropical cyclones [3], [4].

In the 1970s, satellite measurements of ocean surface parameters started by using infrared (IR) radiometers aboard the National Oceanic and Atmospheric Administration's (NOAA) geostationary and polar orbiting platforms [5]. Although IR sensors provide measurements with relatively high spatial resolution, they cannot penetrate clouds and aerosols, the thing that limits the utility of their measurements under all weather conditions. As a solution, microwave sensors (both active and passive) came into play and provided researchers with a clear view of the ocean surface, except for rain. This made it possible to produce a reliable time series of sea surface parameters, and offered unprecedented data on both short- and long-term temporal scales with near-global coverage to be used in various climate studies, e.g., [6], [7].

Manuscript received December 14, 2016; revised May 23, 2017 and July 7, 2017; accepted July 31, 2017. (*Corresponding Author: Suleiman Odeh Alswiss.*)

The authors are with the Center for Satellite Applications and Research, National Environmental Satellite, Data, and Information Service, National Oceanic and Atmospheric Administration, College Park, MD 20740 USA (e-mail: [suleimanalswiss@gmail.com](mailto:suleimanalswiss@gmail.com); [zorana.jelenak@noaa.gov](mailto:zorana.jelenak@noaa.gov); [paul.s.chang@noaa.gov](mailto:paul.s.chang@noaa.gov)).

Color versions of one or more of the figures in this paper are available online at <http://ieeexplore.ieee.org>.

Digital Object Identifier 10.1109/JSTARS.2017.2737470

For frequencies up to 11 GHz, the surface radiance is primarily proportional to ocean surface parameters. Until 1997, when the Tropical Rainfall Measuring Mission (TRMM) spacecraft was launched [8] with the TRMM Microwave Imager (TMI) aboard, the usefulness of early radiometers was obstructed by their poor calibration systems or the lack of low-frequency channels sensitive to sea surface parameters. TMI acquired radiances from a wide range of frequencies (from 10 up to 85 GHz) and represented the first space-based microwave sensor that was capable of accurately measuring SST through clouds. A few years later in January 2003, the Naval Research Laboratory Remote Sensing Division and the Naval Center for Space Technology for the U.S. Navy and the National Polar-Orbiting Operational Environmental Satellite System Integrated Program Office, launched the WindSat Polarimetric Radiometer that was capable of measuring ocean surface wind vectors and SST in addition to several geophysical parameters.

In May 2012, the Japanese Aerospace Exploration Agency (JAXA) launched the Global Change Observation Mission-Water (GCOM-W1) with the Advanced Microwave Scanning Radiometer-2 (AMSR-2) onboard [9]. AMSR-2 has a full suite of channels ranging from 6 to 89 GHz providing sufficient information to retrieve ocean surface parameters.

In this paper, we will present a retrieval algorithm currently implemented at NOAA, through the GCOM-W1 AMSR-2 Algorithm Software Processor, to operationally generate and make available of the AMSR-2 sensor and environmental data records (SDRs and EDRs, respectively) as part of the GCOM-W1 Processing and Distribution System (GPDS). We will start with a brief overview of the AMSR-2 instrument in Section II, followed by description of the retrieval algorithm and performance evaluation in Sections III and IV, respectively. Finally, summary and conclusions will be presented in Section V.

## II. AMSR-2 INSTRUMENT OVERVIEW

The GCOM program is part of JAXA's broader commitment toward global and long-term observation of the Earth's environment. GCOM consists of two medium-size polar-orbiting satellite series with one-year overlap between them for inter-calibration. The two satellite series are GCOM-W (Water) and GCOM-C (Climate).

AMSR-2 was selected as a payload on GCOM-W mission to collect observations related to the global water and energy cycle [10]. AMSR-2 is a microwave radiometer system that measures dual polarized [vertical (V-pol) and horizontal (H-pol)] radiances at 6.9, 7.3, 10.65, 18.7, 23.8, 36.5, and 89.0 GHz. It is a

TABLE I  
AMSR-2 INSTRUMENT SPECIFICATIONS

Center Freq. (GHz)	3-dB Beam Width (deg.)	Ground IFOV (km)	Sampling Interval (km)
6.925/7.3	1.8	35 × 62	10
10.65	1.2	24 × 42	
18.7	0.65	14 × 22	
23.8	0.75	15 × 26	
36.5	0.35	7 × 12	
89.0	0.15	3 × 5	5

sun-synchronous orbiter (local time of ascending node 13:30) with a conical scanning geometry to obtain measurements along a semicircular pattern in front of the spacecraft. It operates at a nominal earth incidence angle of  $55^\circ$  resulting in a wide swath of 1450 km [11], [12]. The summarized instrument specifications of AMSR-2 are shown in Table I.

### III. ALGORITHM DESCRIPTION

Passive microwave radiometers are capable of measuring several geophysical parameters including SST. It has been noticed that the sensitivity of surface radiances is proportional to surface parameters for frequencies up to 11 GHz. In particular, for microwave frequency range of 4–8 GHz, the dielectric constant for water changes with physical temperature, resulting in changes in the emissivity values up to  $\sim 50\%$ . For higher frequencies, surface radiances become less sensitive to changes in surface parameters [13], but they provide important information about the atmosphere above the surface.

Since the SST retrieval algorithm described in this paper is a statistical-based algorithm, we found that including AMSR-2 measurements from frequencies up to 36 GHz will cover more variability and improve the goodness of the multivariate regression models used in the algorithm.

#### A. Observed Brightness Temperatures

The algorithm utilizes AMSR-2 Tbs obtained from 12 different AMSR-2 channels (H- and V-pol 6.9, 7.3, 10.65, 18.7, 23.8, and 36.5 GHz). These Tbs are obtained from JAXA's Level 1B version 1.1 (GW1AM2 L1B v1.1, denoted hereafter as L1B) released on March 1, 2013. In addition to observed Tbs, this data product contains the observation position (latitude, longitude), time, and orbit information. The product summary and description is available online in [14].

These recorded AMSR-2 L1B Tbs were corrected using the approach described in [9] to reduce post-launch residual calibration biases. It is obvious that using corrected AMSR-2 Tbs in oceanic geophysical retrieval algorithms will significantly improve the quality and accuracy of the retrieved geophysical parameters and the efficacy of the algorithm itself.

#### B. Quality Control (QC)

The measured Tbs from a microwave radiometer are affected by various surface and atmospheric parameters. The algorithm accounts for several surface parameters namely: wind speed

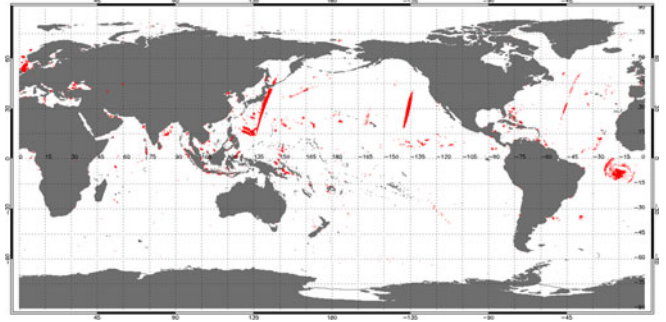


Fig. 1. Example of the spatial pattern of points flagged due to RFI.

( $ws$ ), wind direction relative to antenna azimuth ( $\chi$ ), land and ice contamination, sun glitter contamination, C-band radio frequency interference (RFI), cross track location of the measurement ( $xtrack_{id}$ ), and total precipitable water (TPW). The effect of salinity is very small, and was not accounted for in the algorithm.

Contaminations due to land and ice were accounted for by flagging the contaminated areas using the L1B land/ice mask. In addition, a more aggressive land/ice mask (100 km off the shoreline) is also included in the ocean EDRs in case users chose to use it.

Furthermore, AMSR-2 ascending orbits are susceptible to significant sun glitter effects. For pixels suffering from sun glitter contamination (when angle between AMSR-2 viewing direction and the sun glitter direction is  $< 25^\circ$ ) the algorithm will flag these regions using sun azimuth and elevation information provided in the L1B data files.

The addition of the 7.3 GHz channel in AMSR-2 allowed for the detection of C-band RFI. RFI signals are usually narrow banded and will only affect one of the C-band channels (6.9 or 7.3 GHz). The algorithm will detect RFI contaminated measurements if the difference between these two channels is  $> 3$  k. The percentage of points flagged due to RFI over ocean is less than 1% of the data, and the spatial pattern of the ocean RFI contamination is shown in Fig. 1.

It is worth noting that SST will still be retrieved in the sun glitter and RFI contaminated areas but will be flagged as bad quality in the QC flag included in the ocean EDR files.

#### C. Ancillary Data

In order to account for some of the surface effects on observed Tbs, additional ancillary data is needed, namely: the optimum interpolation sea surface temperature (or daily OISST), and the global forecast system (GFS).

The NOAA  $1/4^\circ$  daily OISST is an analysis constructed by blending measurements from different platforms (satellites, ships, buoys) on a regular global grid. A spatially complete SST global map is produced by interpolation to fill in gaps. The basic daily OISST methodology is described in [15], but minor modifications were introduced in the current version, version 2 [16], to compensate for platform differences and sensor biases.

The daily OISST belongs to a family of products at the National Centers for Environmental Prediction (NCEP) that

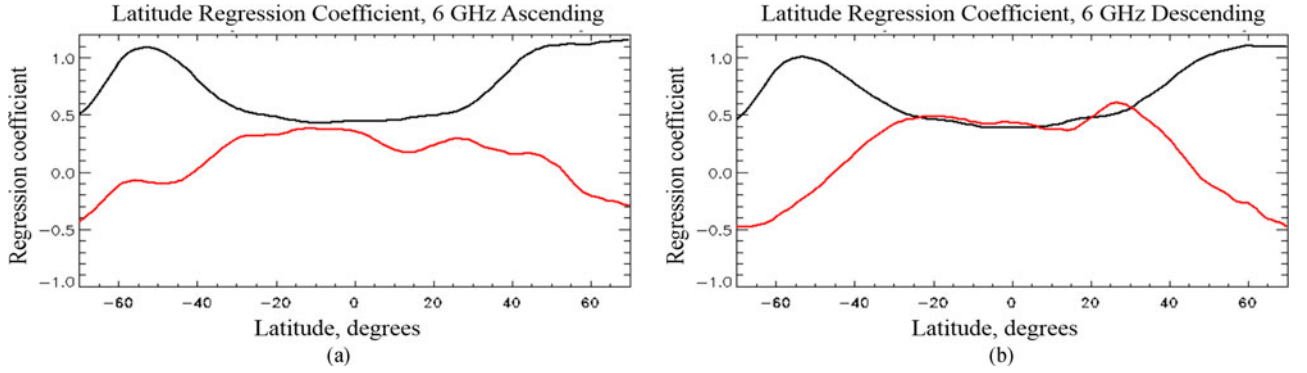


Fig. 2. Example of the regression coefficient ( $a_i$ ) as a function of latitude in degrees for (a) ascending 6 GHz H-pol (red) and V-pol (black) channels, and (b) descending 6 GHz H-pol (red) and V-pol (black) channels.

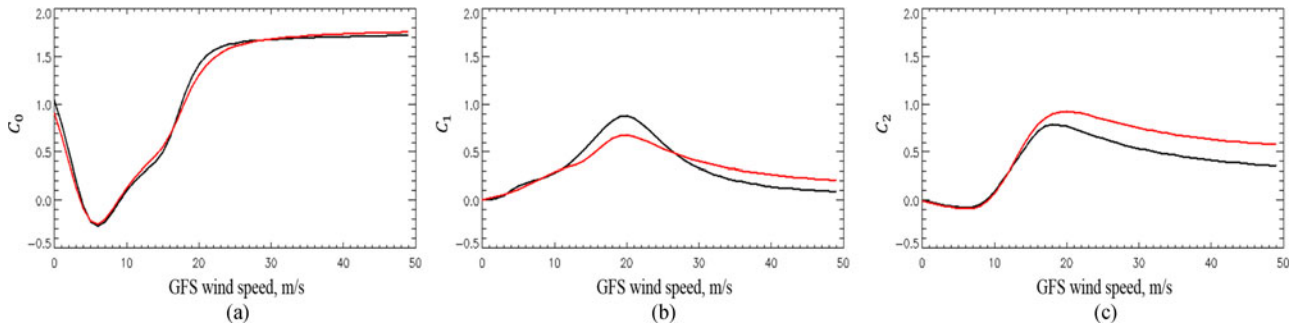


Fig. 3.  $W_s$  correction coefficients as a function of GFS  $w_s$ : (a)  $C_0$ , (b)  $C_1$ , and (c)  $C_2$ , for ascending (red) and descending (black) AMSR-2 measurements.

is sometimes referred to as ‘‘Reynolds SST.’’ There are two kinds of daily OISST, named after the relevant satellite SST sensors. These are the advanced very high resolution radiometer (AVHRR) and Advanced Microwave Scanning Radiometer on the Earth Observing System (AMSR-E). AVHRR has the longest record (from late 1981 to the present) of SST measurements from a single sensor, and was used in this study.

The second ancillary data source required is the GFS model. GFS is a coupled weather forecast model produced by NCEP and composed of four separate models (an atmosphere model, an ocean model, a land/soil model, and a sea ice model). Dozens of atmospheric, ocean, and land-soil variables are available through this dataset, from temperatures, winds, and precipitation to soil moisture and atmospheric ozone concentration. The entire globe is covered by the GFS at a base horizontal resolution of 18 miles ( $\sim 28$  km) between grid points, which is commonly used by operational forecasters who predict weather out to 16 days in the future. The daily global 28 km resolution GFS maps were used to provide necessary global  $w_s$  and wind direction information for the algorithm.

All ancillary global fields were spatially and temporally interpolated to AMSR-2 observation time and location before being fed to the retrieval algorithm, and are included, for convenience, in AMSR-2 ocean EDR data products.

#### D. Algorithm Theoretical Basis

The retrieval algorithm described here consists of several steps to infer the desired SST from AMSR-2 observations.

First, we divided the data into  $3^\circ$  latitude bins with 50% overlap between bins. For each latitude bin, 12 AMSR-2 channels (6–36 GHz, H- and V-pol) were used in the localized multivariate regression against Reynolds SST to retrieve preliminary SST ( $SST_{prelim}$ ) as follows:

$$SST_{prelim} = \sum_{i=1}^{12} a_i T b_i \quad (1)$$

where  $T b_i$  is the observed Tb for 6, 7, 10, 18, 23, and 36 GHz H- and V-pol. The regression coefficients  $a_i$  are a function of latitude, frequency, polarization, and they are also different for ascending and descending AMSR-2 measurements. In addition to having 50% overlapping between latitude bins, regression coefficients were smoothed using spline method to avoid any discontinuity in regression models output. Fig. 2 shows an example of the  $a_i$  coefficient as a function of latitude in degrees for (a) ascending 6 GHz H-pol (red) and V-pol (black) channels, and (b) descending 6 GHz H-pol (red) and V-pol (black) channels.

Since microwave emission of the ocean depends on surface roughness, when the surface becomes more rough, the emission increases and becomes less polarized [17], [18]. The wind induced roughness of the ocean surface is driven by  $w_s$  and wind direction relative to the antenna azimuth of the instrument ( $\chi$ ). However, due to the fact that the height of capillary waves is very anisotropic [19], the capillary waves traveling in the up-wind direction have a greater amplitude than those traveling

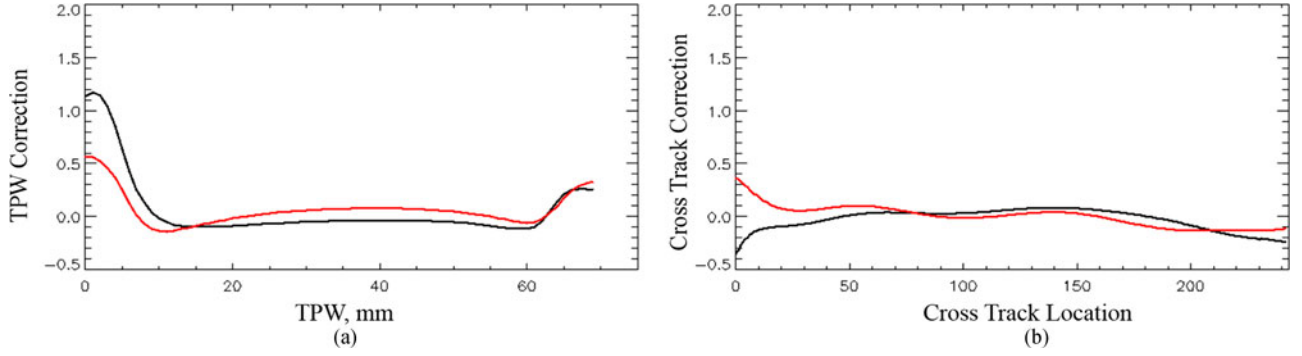


Fig. 4. (a) TPW and (b) cross track location correction to SST values for ascending (red) and descending (black) AMSR-2 measurements.

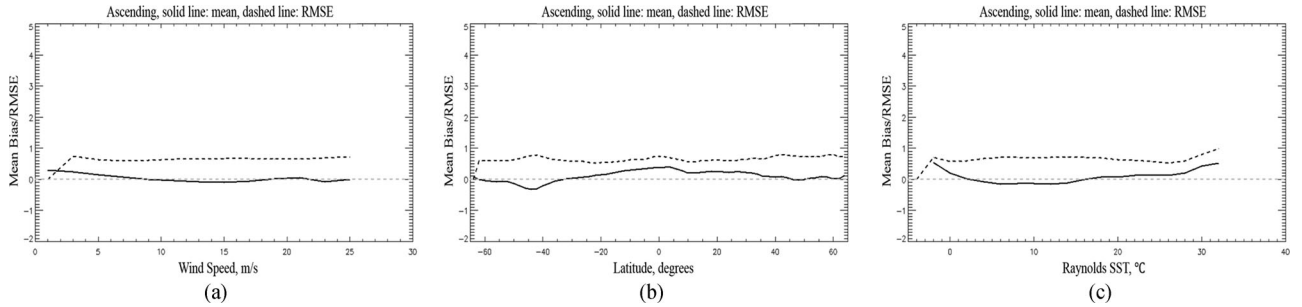


Fig. 5. Comparison between the retrieved SST and Reynolds' SST for ascending AMSR-2 measurements. The y-axis is the mean and RMS SST error ( $SST_{\text{retrieved}} - SST_{\text{Reynolds}}$ ), and the x-axis is (a) GFS  $w_s$ , (b) latitude, and (c) Reynolds' SST. Solid lines represent the mean error and the dashed lines represent the RMS error.

in the crosswind direction resulting in an upwind-downwind asymmetry in the sea-surface emissivity [20], [21].

Thus, the next step in the algorithm is to correct the output of the regression models ( $SST_{\text{prelim}}$ ) for  $w_s$  and relative wind direction effects. This requires modeled wind field that is obtained from the interpolated GFS maps, and AMSR-2 antenna azimuth measurements from the L1B data. The wind effect correction ( $SST_{\text{wind}}$ ) can be mathematically expressed as follows:

$$SST_{\text{wind}} = C_0 + C_1 \cos(\chi) + C_2 \cos(2\chi). \quad (2)$$

As can be noted, (2) consists of two parts: a dc offset ( $C_0$ ), which is a function of  $w_s$ , and an anisotropic term that represents the dependence on  $\chi$ . The latter term is modeled using a first- and second-harmonic cosine functions of  $\chi$  where the  $C_1$  and  $C_2$  coefficients vary with  $w_s$  as well. Fig. 3 shows the coefficients  $C_0$  (panel a),  $C_1$  (panel b), and  $C_2$  (panel c) for ascending (red) and descending (black) AMSR-2 measurements.

Afterwards, SST values undergo another secondary set of corrections to account for TPW and cross track location. The purpose of the TPW correction is to mitigate the atmospheric effect on SST retrievals; while the cross track location correction will help to overcome some cross track location dependent calibration biases in AMSR-2 measured Tbs. The TPW values used in the correction functions are retrieved from AMSR-2 measurements. Fig. 4 shows the corrections for (a) TPW and (b) cross track location for both ascending (red) and descending (black) AMSR-2 measurements.

Finally, a  $(5 \times 5)$  sliding window cumulative distribution function (CDF) smoothing was implemented followed by a median filter to suppress noise. The CDF smoothing step is

implemented on the retrieved SST values with more than  $2^\circ\text{C}$  RMS error when compared to modeled SST values obtained from Reynolds' SST model. It is worth mentioning that regression models and corrections were developed using one-year worth of data (2015) from AMSR-2, GFS, and Reynolds' SST. All the corrections applied to the retrieved SST combined are in the order of  $\sim 10\%$  of the SST range and are subtracted from  $SST_{\text{prelim}}$ . The retrieved SST will have the same spatial resolution as the Tb measurements provided in the L1B data which is  $0.1^\circ$ .

#### IV. RESULTS VALIDATION

To validate the results of the algorithm, we compared the retrieved SST with models and other *in situ* SST measurements. Six months of independent data (January – June of 2014) were used in the validation process presented in this section.

Figs. 5 and 6 show a comparison between retrieved SST and Reynolds' SST for ascending and descending AMSR-2 measurements, respectively. The y-axis is the mean and RMS SST error ( $SST_{\text{retrieved}} - SST_{\text{Reynolds}}$ ), and the x-axis is (a) GFS  $w_s$ , (b) latitude, and (c) Reynolds' SST. The solid lines represent the mean error, and the dashed line represents the RMS error. However, since Reynolds SST was used to train the first step of the regression, systematic errors may not appear in this comparison.

Next, the retrieved SST values were compared to similar SST products provided by JAXA Level-2 data [22] and remote sensing systems (RSS) version 7.2 (V7.2) data [23]. Figs. 7 and 8 show the three-dimensional (3-D) density plot, for ascending and descending orbits, with SST error (SST product - Reynolds)

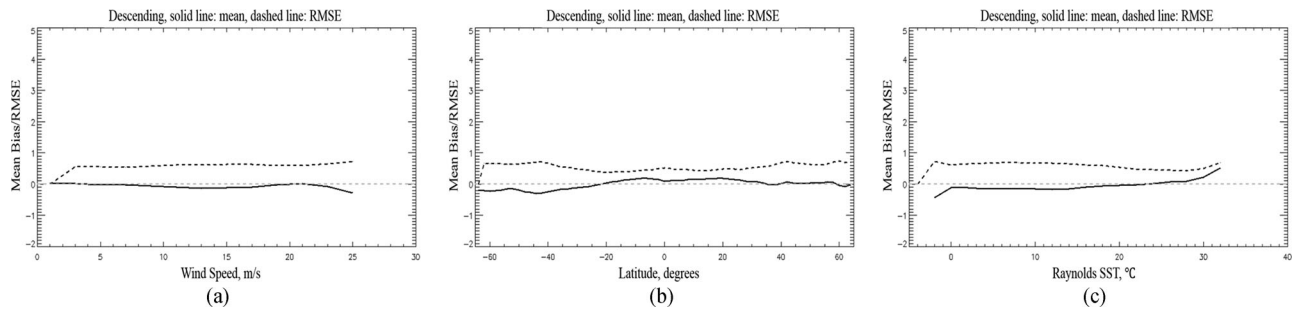


Fig. 6. Comparison between the retrieved SST and Reynolds' SST for descending AMSR-2 measurements. The y-axis is the mean and RMS SST error ( $SST_{\text{retrieved}} - SST_{\text{Reynolds}}$ ), and the x-axis is (a) GFS  $w_s$ , (b) latitude, and (c) Reynolds' SST. Solid lines represent the mean error and the dashed lines represent the RMS error.

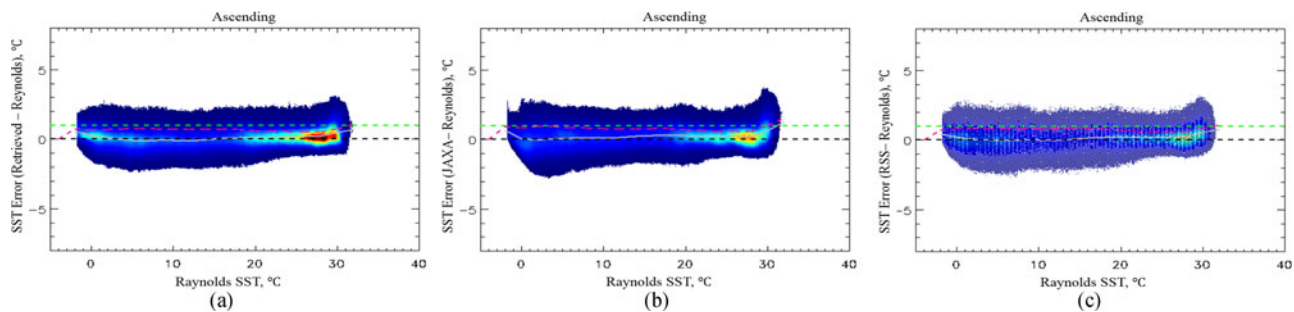


Fig. 7. Comparison between different SST products and Reynolds' SST for ascending AMSR-2 measurements. The x-axis is Reynolds SST, and the y-axis is the SST error for (a) NOAA SST, (b) JAXA SST, and (c) RSS SST. Solid grey lines represent the mean error and the magenta dashed lines represent the RMS error. The dashed black and green lines are the 0 °C and 1 °C, respectively, plotted to serve as a reference.

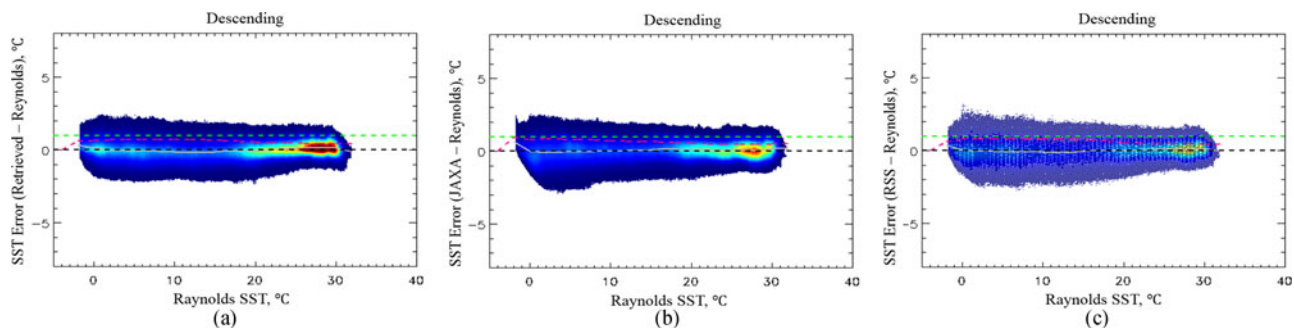


Fig. 8. Comparison between different SST products and Reynolds' SST for descending AMSR-2 measurements. The x-axis is Reynolds SST, and the y-axis is the SST error for (a) NOAA SST, (b) JAXA SST, and (c) RSS SST. Solid grey lines represent the mean error and the magenta dashed lines represent the RMS error. The dashed black and green lines are the 0 °C and 1 °C, respectively, plotted to serve as a reference.

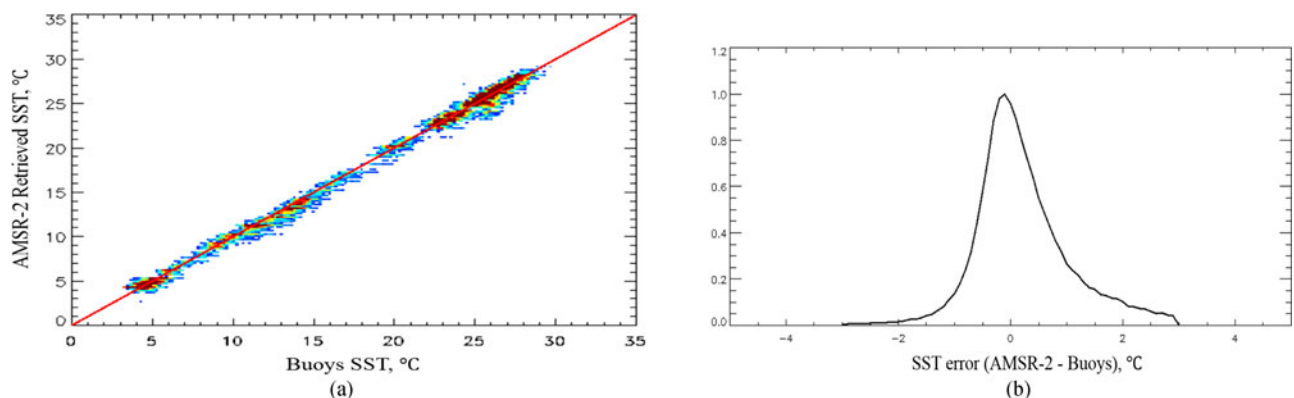


Fig. 9. AMSR-2 SST comparison with buoys. (a) 3-D scatter plot with AMSR-2 SST retrievals on the y-axis and buoys SST measurements on the x-axis. Color denotes the density of points where warmer colors indicate more points. (b) Histogram of the SST error ( $SST_{\text{retrieved}} - SST_{\text{Buoy}}$ ).

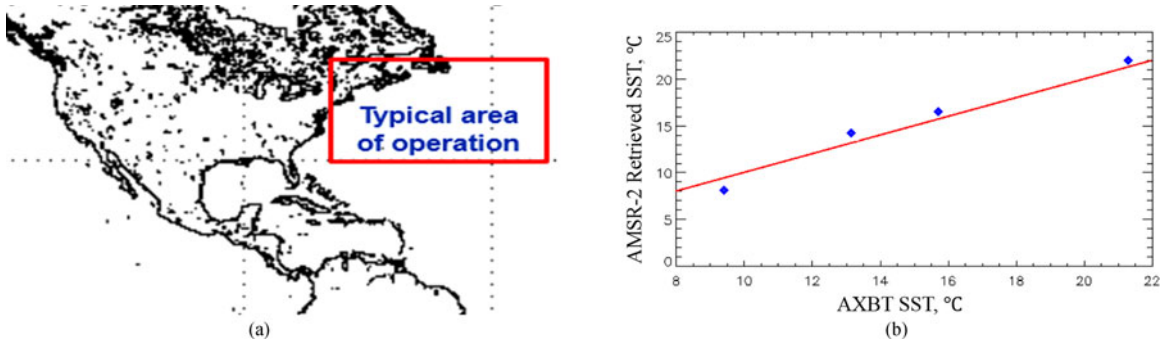


Fig. 10. Comparing AMSR-2 SST with AXBT measured SST during 2016 winter season field experiment campaign. (a) Shows the typical area of operation and (b) shows the scatter plot with the AXBT measured SST on the  $x$ -axis and AMSR-2 retrieved SST on the  $y$ -axis.

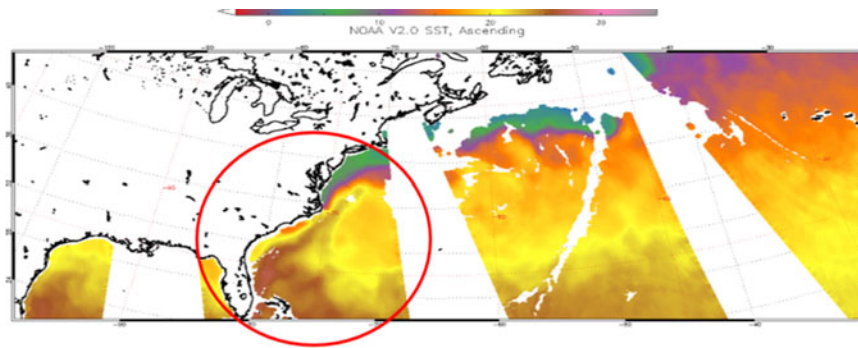


Fig. 11. Example of the Gulf Stream captured by AMSR-2 SST retrievals on April 1, 2014.

on the  $y$ -axis and Reynolds SST on the  $x$ -axis. Color denotes the density of points where warmer colors indicate more points. It is clear that the error analysis for all three products is very similar when compared to Reynolds SST.

Moreover, we compared AMSR-2 SST retrievals with buoy SST measurements. Buoy data are from NOAA's National Centers for Environmental Information, and include information from both moored and drifting buoys. The number of collocated observations is  $\sim 2000$  points with collocation criteria of 10 km maximum distance and 10 min maximum time difference between measurements and the buoy must be at least 100 km away from coast. Fig. 9(a) shows the 3-D scatter plot with AMSR-2 SST retrievals on the  $y$ -axis and buoys SST measurements on the  $x$ -axis. Color denotes the density of points where warmer colors indicate more points. It is clear that the two SST values are in excellent agreement being clustered around the perfect agreement line (red line). Fig. 9(b) shows the histogram of the SST error ( $SST_{\text{retrieved}} - SST_{\text{Buoys}}$ ), where it shows that the mean error is around ( $-0.1$  °C).

During the 2016 winter season field experiment campaign performed by NOAA, we dropped several Airborne eXpendable Bathy Thermograph (AXBT) to collect SST measurements from the Atlantic Ocean. They were timed to coincide with AMSR-2 overpass within 2-h time window. Fig. 10(a) shows the typical region of operation for the field experiment campaign, and Fig. 10(b) shows the scatter plot with the AXBT measured SST on the  $x$ -axis and AMSR-2 retrieved SST on the  $y$ -axis. Unfortunately, the failure rate for these AXBT was very high and we ended up with four point measurements only. The

closest AMSR-2 measurements to the location of the AXBTs hitting the surface were chosen for comparison.

Finally, Fig. 11 shows an example of the Gulf Stream captured by AMSR-2 SST retrievals on April 1, 2014.

## V. SUMMARY

In this paper, we presented a statistical-based SST retrieval algorithm from AMSR-2 observations. This algorithm is currently implemented and operational through GPDS at NOAA. The algorithm utilizes observations from 12 AMSR-2 channels, in addition to ancillary data to retrieve SST.

After retrieving a preliminary SST values, they undergo a set of corrections to account for other parameters that affect the emissivity of the ocean. The algorithm accounts for  $ws$  and relative wind direction effect, contamination from land, ice, and RFI, TPW effect, and cross track location inside the AMSR-2 swath.

To validate the retrieved AMSR-2 SST values, we compared them with models (Reynolds' SST), other AMSR-2 SST data products from JAXA and RSS, buoys, and AXBTs. Results show that the retrieved SSTs are in excellent agreement with other measurement with a mean error of  $0.2$  °C, and an RMS error of  $0.6$  °C.

## ACKNOWLEDGMENT

The views expressed in this paper are those of the authors and must not be interpreted as those of National Oceanic and Atmospheric Administration (NOAA) or the U.S. Government.

## REFERENCES

- [1] M. A. Cane, S. E. Zebiak, and S. C. Dolan, "Experimental forecasts of El Niño," *Nature*, vol. 321, pp. 827–832, 1986.
- [2] M. J. McPhaden, "Genesis and evolution of the 1997-1998 El Niño," *Science*, vol. 283, pp. 950–954, 1999.
- [3] M. DeMaria and J. Kaplan, "Sea surface temperature and the maximum intensity of Atlantic tropical cyclones," *J. Climate*, vol. 7, pp. 1324–1334, 1994.
- [4] K. A. Emanuel, "Thermodynamic control of hurricane intensity," *Nature*, vol. 401, pp. 665–669, 1999.
- [5] E. P. McClain, W. G. Pichel, and C. C. Walton, "Comparative performance of AVHRR-based multichannel sea surface temperatures," *J. Geophys. Res.*, vol. 90, pp. 11587–11601, 1985.
- [6] N. C. Gordy, "Remote sensing of atmospheric water content from satellites using microwave radiometry," *IEEE Trans. Antennas Propag.*, vol. AP-24, pp. 155–162, 1976.
- [7] T. T. Wilheit and A. T. C. Chang, "An algorithm for retrieval of ocean surface and atmospheric parameters from the observations of the scanning multichannel microwave radiometer," *Radio Sci.*, vol. 15, pp. 525–544, 1980.
- [8] C. Kummerow, W. Barnes, T. Kozu, J. Shiue, and J. Simpson, "The tropical rainfall measuring mission (TRMM) sensor package," *J. Atmos. Ocean. Technol.*, vol. 15, pp. 808–816, 1998.
- [9] S. O. Alswiess, Z. Jelenak, P. S. Chang, J. D. Park, and P. Meyers, "Inter-calibration results of the advanced microwave scanning radiometer-2 over ocean," *IEEE J. Sel. Topics Appl. Earth Observ. Remote Sens.*, vol. 8, no. 9, pp. 4230–4238, Sep. 2015.
- [10] Overview of The Global Change Observation Mission (GCOM). [Online]. Available: [http://suzaku.eorc.jaxa.jp/GCOM\\_W/w\\_amsr2/GCOM\\_RA\\_3rd\\_Guide\\_AppendixC.pdf](http://suzaku.eorc.jaxa.jp/GCOM_W/w_amsr2/GCOM_RA_3rd_Guide_AppendixC.pdf).
- [11] JAXA GCOM-W1. [Online]. Available: [http://suzaku.eorc.jaxa.jp/GCOM\\_W/w\\_amsr2/whats\\_amsr2.html](http://suzaku.eorc.jaxa.jp/GCOM_W/w_amsr2/whats_amsr2.html).
- [12] K. Imaoka, M. Kachi, M. Kasahara, N. Ito, K. Nakagawa, and T. Oki, "Instrument performance and calibration of AMSR-E and AMSR2," in *Proc. Int. Conf. Archives Photogrammetry Remote Sens. Spatial Inf. Sci.*, Kyoto, Japan, 2010, vol. XXXVIII.
- [13] J. P. Hollinger and R. C. Lo, "Determination of sea surface temperature with N-ROSS," Naval Res. Laboratory Memorandum, Washington, DC, USA, Tech. Rep. 5375, 1984.
- [14] AMSR-2 Level1 Product. [Online]. Available: [ftp://suzaku.eorc.jaxa.jp/pub/AMSR2/public/Format/AMSR2\\_Level1\\_Product\\_Format\\_EN.pdf](ftp://suzaku.eorc.jaxa.jp/pub/AMSR2/public/Format/AMSR2_Level1_Product_Format_EN.pdf)
- [15] R.W. Reynolds, T. M. Smith, C. Liu, D. B. Chelton, K. S. Casey, and M. G. Schlax, "Daily high-resolution-blended analyses for sea surface temperature," *J. Climate*, vol. 20, pp. 5473–5496, 2007.
- [16] [Online]. Available: [https://www.ncdc.noaa.gov/sites/default/files/attachments/Reynolds2009\\_oisst\\_daily\\_v02r00\\_version2-features.pdf](https://www.ncdc.noaa.gov/sites/default/files/attachments/Reynolds2009_oisst_daily_v02r00_version2-features.pdf)
- [17] S. T. Wu and A.K. Fung, "A noncoherent model for microwave emission and backscattering from the sea surface," *J. Geophys. Res.*, vol. 77, pp. 5917–5929, 1972.
- [18] F. J. Wentz, "A two-scale scattering model for foam-free sea microwave brightness temperatures," *J. Geophys. Res.*, vol. 80, pp. 3441–3446, 1975.
- [19] H. Mitsuyasu and T. Honda, "Wind-induced growth of water waves," *J. Fluid Mech.*, vol. 123, pp. 425–442, 1982.
- [20] F. J. Wentz, "Measurement of oceanic wind vector using satellite microwave radiometers," *IEEE Trans. Geosci. Remote Sens.*, vol. 30, no. 5, pp. 960–972, Sep. 1992.
- [21] T. Meissner and F. J. Wentz, "An updated analysis of the ocean surface wind direction signal in passive microwave brightness temperature," *IEEE Trans. Geosci. Remote Sens.*, vol. 40, no. 6, pp. 1230–1240, Jun. 2002.
- [22] JAXA Products: Definition of Processing Levels. [Online]. Available: [http://suzaku.eorc.jaxa.jp/GCOM\\_W/data/data\\_w\\_product-1.html](http://suzaku.eorc.jaxa.jp/GCOM_W/data/data_w_product-1.html)
- [23] F. J. Wentz, T. Meissner, C. Gentemann, K.A. Hilburn, and J. Scott, Remote Sensing Systems GCOM-W1 Daily Environmental Suite on 0.25 deg grid, Version 7.2, SST. Remote Sensing Systems, Santa Rosa, CA, USA, 2014. [online]. Available: [www.remss.com/missions/amsr2](http://www.remss.com/missions/amsr2)



**Suleiman Odeh Alswiess** (S'05–M'11) received the Ph.D. degree in electrical engineering from the University of Central Florida, Orlando, FL, USA, in 2011.

Then, he joined the Center for Satellite Applications and Research, National Environmental Satellite, Data and Information Service, part of the National Oceanic and Atmospheric Administration, as a support Scientist with Global Science & Technology Inc., where he worked on sensors calibration, and advanced satellite data products development and validation. In 2016, he joined Florida Polytechnic University, Lakeland, FL, USA, as an Assistant Professor of electrical engineering where he continues to conduct research in microwave remote sensing and earth observing systems.



**Zorana Jelenak** (S'97–M'04) received the Ph.D. degree in physics from Waikato University, Hamilton, New Zealand, in 2000.

She joined Ocean Winds Team at NOAA/NESDIS /ORA as a UCAR Visiting Scientist in 2001. She is a member of the NASA Ocean Surface Winds science team, NOAA's EDR algorithm lead for AMSR-2 radiometer, and a member of NASA CYGNSS science team. Her research interests include ocean surface wind vector measurements from active and passive microwave measurements and its applicability in an operational near-real time environment, retrieval algorithm development, model function development, advanced statistical analysis, and error analysis for improved algorithm characterization.



**Paul S. Chang** (S'87–M'90) received the B.S. degree in electrical engineering from Union College, Schenectady, NY, USA, in 1988, and the Ph.D. degree in electrical engineering from the University of Massachusetts, Amherst, MA, USA, in 1994.

Since 1994, he has been a Research Physical Scientist at the Center for Satellite Applications and Research, National Environmental Satellite, Data and Information Service (NESDIS), National Oceanic and Atmospheric Administration (NOAA), Silver Spring, MD, USA. His research interests include research and development in active and passive microwave remote sensing of the ocean surface with an emphasis on retrieval of the ocean surface wind field. Wind retrieval algorithm improvements and new product developments are pursued through the analyses of satellite and aircraft microwave remote sensing data. An emphasis is placed on transitioning research results into operational use, which involves cooperative relationships with the operational facets of NESDIS and with the National Weather Service, a primary end user of this data. His current efforts are focused on working on the METOP, ScatSat, CYGNSS, and GCOM-W missions in addition to planning and risk reduction activities for future ocean vector winds missions.